

# Defect Engineering in Two Common Types of Dielectric Materials for Electromagnetic Absorption Applications

Bin Quan, Wenhao Shi, Samuel Jun Hoong Ong, Xiaochi Lu, Paul Luyuan Wang, Guangbin Ji,\* Yufeng Guo,\* Lirong Zheng, and Zhichuan J. Xu\*

Dielectric materials are greatly desired for electromagnetic absorption applications. Lots of research shows that conduction loss and polarization are two of the most important factors determining complex permittivity. However, the detailed dissipation mechanisms for the improved microwave absorption performance are often based on semiempirical rules, lacking practical data relationships between conduction loss/polarization and dielectric behaviors. Here, a strategy of introducing point defects is used to understand such underlying relationships, where polarizability and conductivity are adjustable by manipulating oxygen deficiency or heteroatoms. Based on first principles calculations and the applied oxygen-deficient strategy, dielectric polarization is shown to be dominant in determining the permittivity behaviors in semiconductors. Meanwhile, the presented nitrogen doping strategy shows that conduction loss is dominant in determining the permittivity behavior in graphitized carbon materials. The validity of the methods for using point defects to explore the underlying relations between conduction loss/polarization and dielectric behaviors in semiconductor and graphitized carbon are demonstrated for the first time, which are of great importance in optimizing the microwave absorption performance by defect engineering and electronic structure tailoring.

(like graphene, graphitized carbon, and semiconductors) are more promising for microwave absorption applications due to their low density, high aspect ratio, fine antioxidation capability, and the ability to be assembled into macroscopic architectures or films. In view of the importance of dielectric materials to improve the microwave absorption performance, lots of researches about dielectrics-based microwave absorption have been done.<sup>[4–6]</sup> Decades of experimental researches have generated a huge body of knowledge on the links between processing and microstructural properties,<sup>[7,8]</sup> as well as how they relate to microwave absorption.<sup>[9,10]</sup> So far, it has been widely recognized that conduction loss and polarization (CaP) are two of the dominant factors in determining complex permittivity.<sup>[11]</sup> However, much of the existing understanding of the relationship between attenuation mechanisms and complex permittivity is based on semiempirical rules. Little research has been reported on the quantitative relationship between CaP and permittivity, as well as the preferred dissipation mechanism in different types of dielectrics (e.g., semiconductor/graphitized carbon, graphene, and so on).<sup>[12,13]</sup>

Here, we present the results supporting a detailed CaP-permittivity relationship that was developed by introducing extrinsic point defects into semiconductors (Sc) and graphitized carbon (GC). An aluminum reduction method was used to prepare a series of semiconductors with abundant oxygen vacancies (D-Sc), as shown in **Scheme 1a**. Introducing oxygen vacancies not only improves the charge density of

relationship between CaP and permittivity, as well as the preferred dissipation mechanism in different types of dielectrics (e.g., semiconductor/graphitized carbon, graphene, and so on).<sup>[12,13]</sup> Here, we present the results supporting a detailed CaP-permittivity relationship that was developed by introducing extrinsic point defects into semiconductors (Sc) and graphitized carbon (GC). An aluminum reduction method was used to prepare a series of semiconductors with abundant oxygen vacancies (D-Sc), as shown in **Scheme 1a**. Introducing oxygen vacancies not only improves the charge density of

## 1. Introduction

With ever-increasing levels of electromagnetic (EM) radiation pollution in the world today, conventional EM absorbing materials with strong absorption performance alone are becoming insufficient for many applications. More stringent requirements for EM wave-absorbing materials such as lighter weight, low-frequency dissipation, and broader absorption bandwidth are necessary.<sup>[1–3]</sup> Compared to traditional easily corroded, narrowbandwidth, and heavy metal materials, dielectric materials

B. Quan, Prof. G. B. Ji  
College of Materials Science and Technology  
Nanjing University of Aeronautics and Astronautics  
Nanjing 210016, China  
E-mail: gbji@nuaa.edu.cn

B. Quan, S. J. H. Ong, Dr. P. L. Y. Wang, Prof. Z. C. J. Xu  
School of Materials Sciences and Engineering  
Nanyang Technological University  
50 Nanyang Avenue, Singapore 639798, Singapore  
E-mail: xuzc@ntu.edu.sg

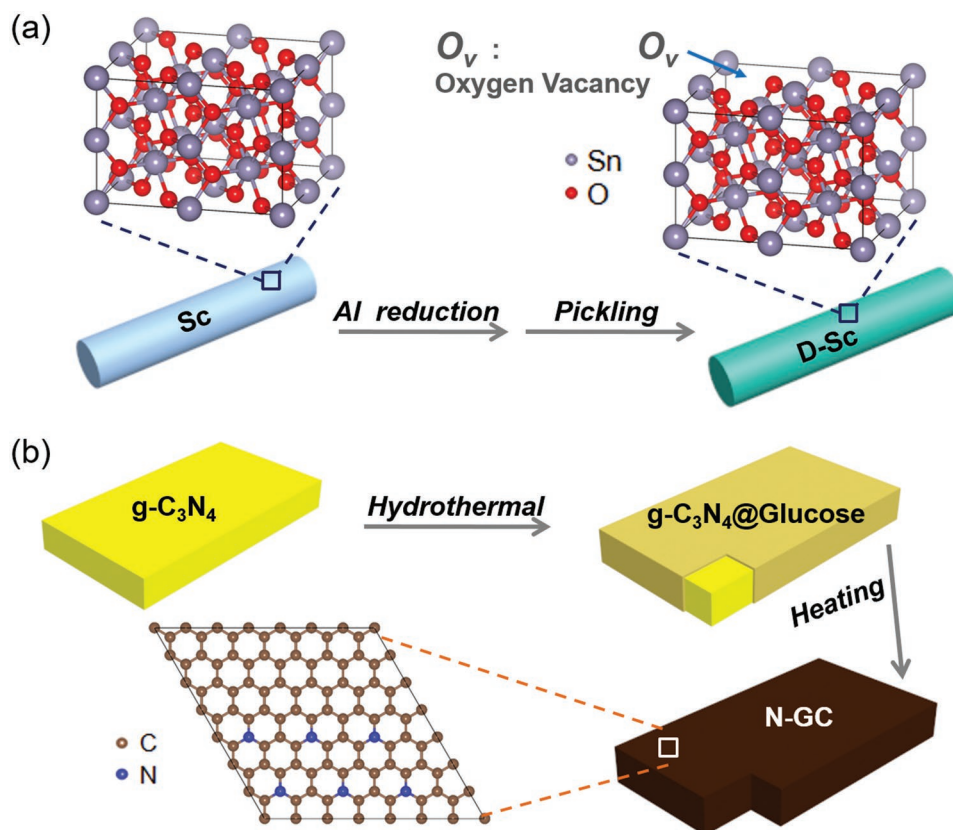
 The ORCID identification number(s) for the author(s) of this article can be found under <https://doi.org/10.1002/adfm.201901236>.

DOI: 10.1002/adfm.201901236

W. H. Shi, Prof. Y. F. Guo  
State Key Laboratory of Mechanics and Control of Mechanical Structures  
College of Aerospace Engineering  
Nanjing University of Aeronautics and Astronautics  
Nanjing 210016, China  
E-mail: yfguo@nuaa.edu.cn

X. C. Lu  
College of Materials Science and Engineering  
Nanjing Tech University  
Nanjing 210009, China

Dr. L. R. Zheng  
Beijing Synchrotron Radiation Facility of the Institute of High Energy Physics  
Chinese Academy of Sciences  
Beijing 100049, China



**Scheme 1.** Schematic illustration of the step-by-step fabrication methods of a) D-Sc and b) N-GC. The gray, red, brown, and blue dots denote Sn, O, C, and N atoms, respectively.

semiconductors around the valence band maximum,<sup>[14]</sup> but also changes the intrinsic bandgap ( $E_g$ ) of the semiconductors.<sup>[15]</sup> Thus, the abundant localized electrons in Sc are expected to result in more polarizations, like dipolar polarization. In addition, the electrical conductivity of semiconductors can also be improved with the variation of  $E_g$ .<sup>[16]</sup> In brief, the proposed oxygen-deficient strategy indicates that dielectric polarization is dominant in determining the permittivity behaviors in Sc. Meanwhile, N-doped GC (N-GC) was obtained by the pyrolysis of nitrogen-rich precursors in inert atmosphere, as shown in Scheme 1b. Introducing electron-rich nitrogen into the carbonaceous materials can improve the electrical conductivity of graphitized carbon by contributing electron lone pairs to the carbon conjugated system or taking positions inside aromatic rings with  $sp^2$  hybridization.<sup>[17]</sup> In addition, the dielectric polarization could also be influenced by the variation of electronic structures. In summary, the presented nitrogen-doping strategy exhibits that conduction loss is dominant in determining the permittivity behaviors in GC.

## 2. Results and Discussion

To explore the relationship between CaP and permittivity behaviors, a series of conventional semiconductors with oxygen vacancies (D-Sc-0.1, aluminothermic reduction with 0.1 g of Al powder) were prepared by the aluminum reduction method.

Their structures were confirmed by X-ray diffraction (XRD) patterns, as seen in Figure S1 (Supporting Information). The frequency-dependence  $\epsilon'$  values between pure Sc and D-Sc-0.1 and related linear change of the average  $\epsilon'$  values from Sc to D-Sc-0.1 are given in Figure S2 (Supporting Information). Interestingly, the obtained D-Sc-0.1 exhibits improved  $\epsilon'$  values with different degrees. The results indicate that oxygen deficiency-induced variation of polarizability and conductivity indeed affects the dielectric behaviors of Sc. In order to further reveal the potential quantitative relation between CaP and permittivity behaviors, more oxygen vacancies were introduced by increasing the reaction dose of nanoaluminum powder. As the feeding amount of aluminum powder was increased from 0.1 to 0.3 g,  $\text{SnO}_2$  is able to maintain its crystal structure (XRD patterns in Figure 1a and transmission electron microscopy (TEM) images in Figure S3 in the Supporting Information). Therefore,  $\text{SnO}_2$  was chosen for further investigating the defect effect due to its relative higher tolerance to high defect amount over other oxides in this work. The detailed structure and composition were investigated by Raman spectra and Fourier transform infrared spectra (FTIR). As shown in Figure 1b,c, D- $\text{SnO}_2$  samples show identical Raman/FTIR profiles as pure  $\text{SnO}_2$ , indicating that aluminum reduction did not induce other impurity phases and basically maintain the original crystal structures of  $\text{SnO}_2$ . The X-ray photoelectron spectroscopy (XPS) spectra in Figure S4 (Supporting Information) reveal the existence of Sn and O elements. In the XPS O 1s spectra, three kinds of

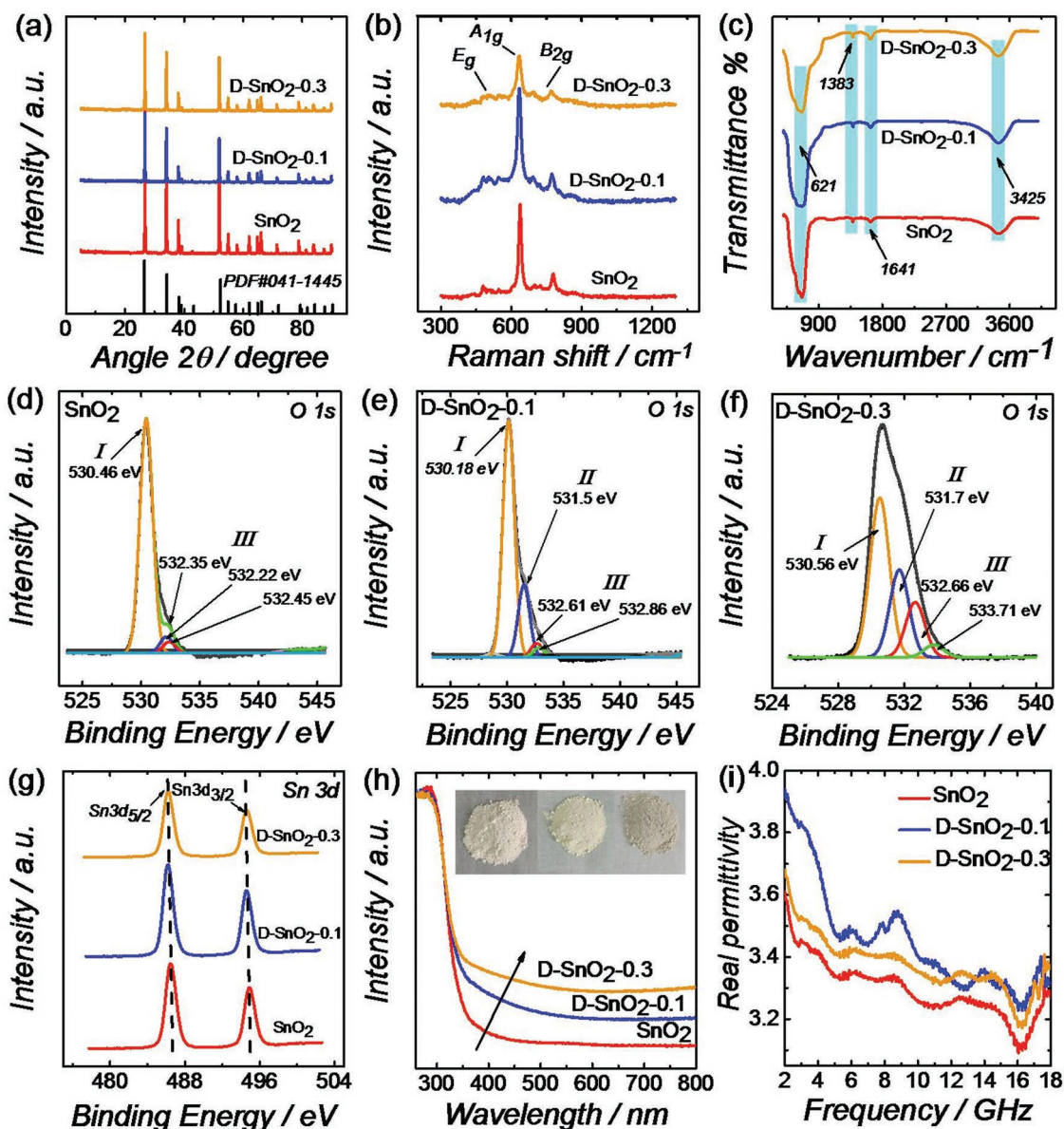


**Figure 1.** a) XRD patterns, b) Raman spectra and c) FTIR spectra of SnO<sub>2</sub>, D-SnO<sub>2</sub>-0.1, and D-SnO<sub>2</sub>-0.3. XPS O 1s spectra of d) SnO<sub>2</sub>, e) D-SnO<sub>2</sub>-0.1, and f) D-SnO<sub>2</sub>-0.3, respectively. g) XPS Sn 3d spectra, h) UV-vis diffuse reflectance spectra, and i) real permittivity of SnO<sub>2</sub>, D-SnO<sub>2</sub>-0.1, and D-SnO<sub>2</sub>-0.3, respectively. The inset in panel (h) shows the photographs of SnO<sub>2</sub>, D-SnO<sub>2</sub>-0.1, and D-SnO<sub>2</sub>-0.3.

peaks can be clearly identified (Figure 1d–f). The peak at 530.37 ( $\pm 0.19$ ) eV (Peak I) can be assigned to the lattice oxygen. The peaks at 531.60 ( $\pm 0.1$ ) eV (Peak II) can be attributed to the O<sup>-</sup> ions in oxygen-deficient regions. The peaks at 532.0–533.0 eV (Peak III) are associated with the surface oxygen.<sup>[18]</sup> The areas of Peak II gradually increase from SnO<sub>2</sub> to D-SnO<sub>2</sub>-0.1 and D-SnO<sub>2</sub>-0.3, indicating the successful generation of oxygen deficiencies as well as a positive correlation between oxygen vacancies and consumed aluminum. In addition, it is noticed that the peak area elevates with the increased oxygen deficiency. This is because that oxygen vacancies and free electrons were generated after SnO<sub>2</sub> was reduced by aluminum.<sup>[19]</sup> Oxygen molecules would be absorbed onto the surface by capturing free electrons from SnO<sub>2-x</sub>.<sup>[18,20]</sup> Therefore, as more oxygen

deficiencies are generated, higher surface oxygen concentration can be observed. In addition, the negligible binding energy shift of Sn 3d spectra (Figure 1g) indicates that introducing oxygen vacancies has little effect on the chemical states of tin. To further confirm the concentration change of oxygen vacancies, UV-vis diffuse reflectance spectra were measured. As shown in Figure 1h, the gradual blueshift of absorption edge and deepening powder color indicate the increased oxygen vacancies concentration from SnO<sub>2</sub> to D-SnO<sub>2</sub>-0.1 and D-SnO<sub>2</sub>-0.3.<sup>[21]</sup> Based on the above results, it can be proved that the D-SnO<sub>2</sub> samples were successfully prepared and oxygen vacancies concentration increases with the increased feeding amount of reductive agent. Interestingly, the obtained complex permittivity ( $\epsilon'$  (Figure 1 i) and  $\epsilon''$  (Figure S5, Supporting Information)) first increases

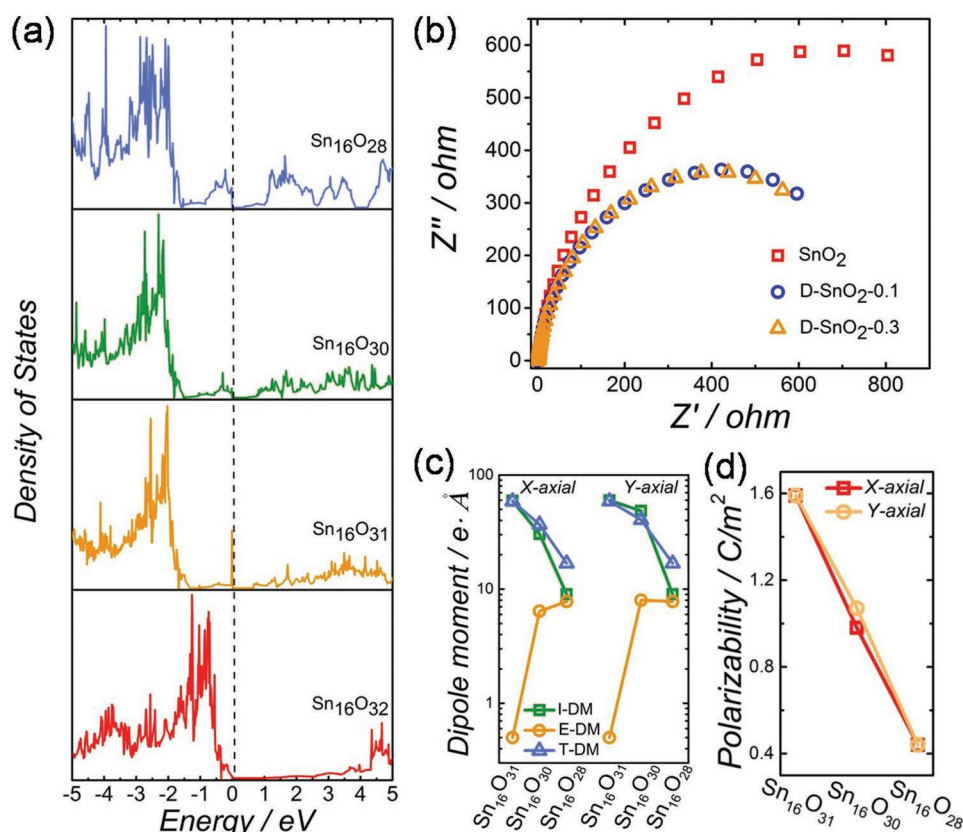


**Figure 2.** a) Density of states of the  $\text{Sn}_{16}\text{O}_{32}$ ,  $\text{Sn}_{16}\text{O}_{31}$ ,  $\text{Sn}_{16}\text{O}_{30}$ , and  $\text{Sn}_{16}\text{O}_{28}$ . b) Nyquist plots of pure  $\text{SnO}_2$ ,  $\text{D-SnO}_2\text{-0.1}$ , and  $\text{D-SnO}_2\text{-0.3}$  with a frequency range from 100 kHz to 10 MHz and an amplitude of 5 mV. The calculated c) dipole moments and d) polarizability in x-axial and y-axial directions of  $\text{Sn}_{16}\text{O}_{31}$ ,  $\text{Sn}_{16}\text{O}_{30}$ , and  $\text{Sn}_{16}\text{O}_{28}$  (dipole moments and polarizability are all expressed with absolute values). I-DM, E-DM, and T-DM stand for ionic dipole moment, electronic dipole moment, and total dipole moment, respectively.

and then decreases. To figure out if this trend is a particular case, similar work for  $\text{TiO}_2$  was done. As can be seen from Figure S6a–d (Supporting Information), the increased oxygen vacancies' concentration of  $\text{TiO}_2$  can be proved by the UV–vis diffuse reflectance spectra and electron paramagnetic resonance (EPR) spectra. In addition, the variation trend of the complex permittivity of  $\text{TiO}_2$  is same with that of  $\text{SnO}_2$ . Based on these findings, it can be inferred that polarization and conduction loss have opposite effects on the permittivity behaviors of semiconductors, e.g.,  $\text{SnO}_2$ ,  $\text{TiO}_2$ ,  $\text{MoS}_2$ , and  $\text{AlN}$ .

To have insight into the effect of oxygen deficiency on the electronic properties, first principles calculations based on density functional theory (DFT) were carried out for bulk  $\text{SnO}_2$  and  $\text{D-SnO}_2$  systems. Four supercell ( $2 \times 2 \times 2$ ) models, including  $\text{Sn}_{16}\text{O}_{32}$  (bulk  $\text{SnO}_2$ ),  $\text{Sn}_{16}\text{O}_{31}$  (3.12% oxygen deficiency),  $\text{Sn}_{16}\text{O}_{30}$  (6.25% oxygen deficiency), and  $\text{Sn}_{16}\text{O}_{28}$  (12.5% oxygen deficiency), were established by removing the lattice oxygen atoms between the interstitial voids as would be the case after aluminum reduction (Figures S7 and S8, Supporting Information). After structural relaxation, some Sn atoms were selected (Figure S9, Supporting Information) and their local density of states (DOSs) were calculated to examine the change in the electronic structures. According to the local DOSs of the selected Sn atoms of the  $\text{Sn}_{16}\text{O}_{32}$ ,  $\text{Sn}_{16}\text{O}_{31}$ ,  $\text{Sn}_{16}\text{O}_{30}$ , and  $\text{Sn}_{16}\text{O}_{28}$  unit cells (Figure S10,

Supporting Information), introducing oxygen deficiencies significantly changes the electronic states around the valence band and the conduction band. As shown from the DOSs in Figure 2a, the bandgaps decrease with the increase of oxygen vacancies. The smaller bandgap indicates the stronger conductivity due to the lower energy barrier for the excitation of charge carriers to conduction band. In view of the dominant role of the bandgap in determining the electrical conductivity of  $\text{Sc}$ ,<sup>[15]</sup> it can be predicted that the conductivity of the materials increases in an order of  $\text{Sn}_{16}\text{O}_{32} < \text{Sn}_{16}\text{O}_{31} < \text{Sn}_{16}\text{O}_{30} < \text{Sn}_{16}\text{O}_{28}$ . The electronic impedance spectra of  $\text{SnO}_2$  and  $\text{D-SnO}_2$  were measured to evaluate the electronic transfer resistance ( $R_{\text{ct}}$ ). As seen from the Nyquist plots in Figure 2b and Figure S11 (Supporting Information), the  $R_{\text{ct}}$  values of  $\text{D-SnO}_2$  are much higher than that of pure  $\text{SnO}_2$ , which indicates the improved electron transport ability after introducing oxygen deficiencies.<sup>[22]</sup> In addition, the slight decrease in size of the semicircle from  $\text{D-SnO}_2\text{-0.1}$  to  $\text{D-SnO}_2\text{-0.2}$  and  $\text{D-SnO}_2\text{-0.3}$  demonstrates the increased conductivity. Therefore, the measured Nyquist plots are in consistency with the theoretical prediction that the electrical conductivity is in an order of  $\text{SnO}_2 < \text{D-SnO}_2\text{-0.1} < \text{D-SnO}_2\text{-0.3}$ . As for the dielectric polarization, it has been proved that the introduction of oxygen vacancies can improve the charge density of  $\text{Sc}$  around the valence band maximum. The abundant localized electrons

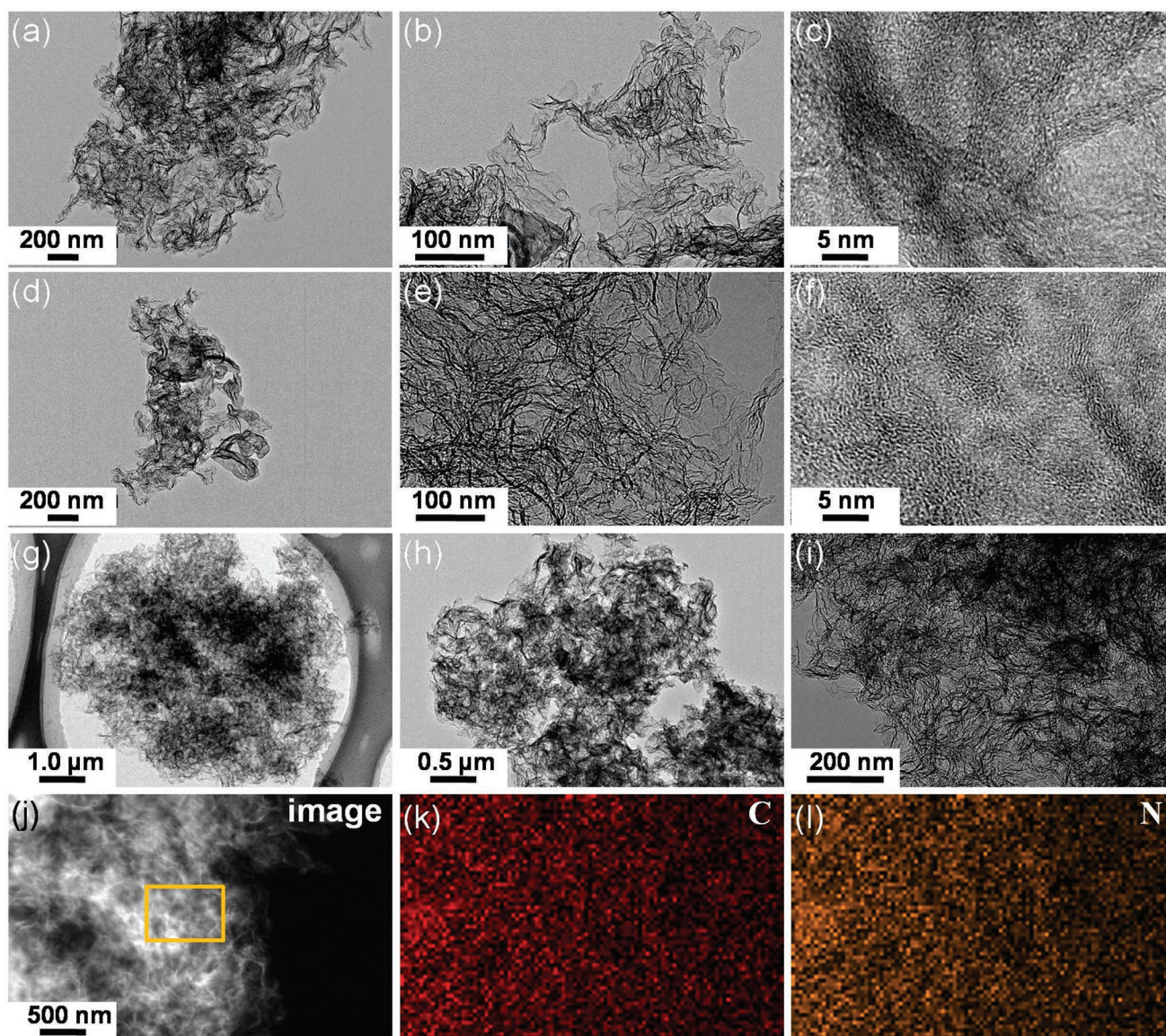


**Figure 3.** TEM and HRTEM images of a–c) N-GC-0.1, d–f) N-GC-0.2, and g–i) N-GC-0.5. j) The selected image with the corresponding elemental mapping of elements k) C and l) N.

in Sc can result in more polarizations, like dipolar polarization. Given that it is difficult to operate and evaluate the practical polarization process in alternating electromagnetic field at GHz, the dipole moments and polarization were estimated using the Berry phase methods implemented in VASP.<sup>[23]</sup> As shown in Figure 2c,d and Table S1 (Supporting Information), the total polarizability along the *x*-axis and *y*-axis of the unit cells decreases with increased oxygen vacancies.

The electrical conductivity order of  $\text{SnO}_2 < \text{D-SnO}_2\text{-}0.1 < \text{D-SnO}_2\text{-}0.3$  has been confirmed based on the theoretical and experimental results. However, the complex permittivity first increases and then decreases from  $\text{SnO}_2$  to  $\text{D-SnO}_2\text{-}0.1$  and  $\text{D-SnO}_2\text{-}0.3$ . It indicates that dielectric polarization and conduction loss have opposite effects on the permittivity behaviors of Sc. In addition, dielectric polarization is dominant in determining the permittivity behaviors.

Thereby, with regard to the relationship between CaP and complex permittivity in Sc, we can come to some conclusions as follows:

- i) In Sc, dielectric polarization and electrical conductivity show directionally opposite effects on the dielectric behaviors.
- ii) In view of the limited conductive capacity of Sc, dielectric polarization is dominant in determining the dielectric behaviors of Sc.

The relation between CaP and permittivity behaviors in graphitized carbon was also explored. Electrical conductivity and polarization were regulated by introducing different contents of nitrogen into graphitized carbon through directly pyrolyzing N-containing  $g\text{-C}_3\text{N}_4/\text{glucose}$  composites. The obtained sheet-like carbon matrix (TEM images in Figure 3a–i) was first

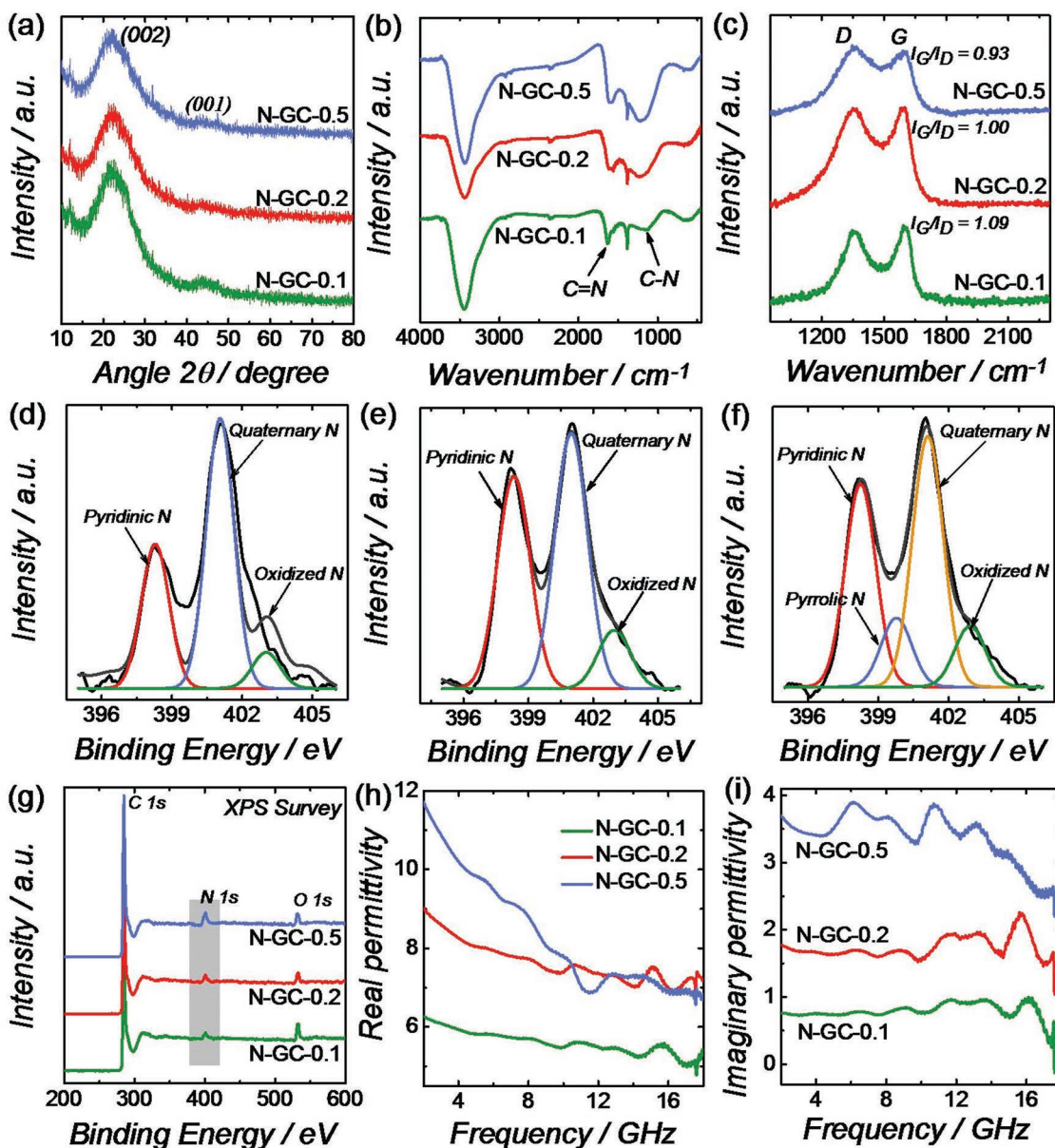


**Figure 4.** a) XRD patterns, b) FTIR spectra, and c) Raman spectra of N-GC-0.1, N-GC-0.2, and N-GC-0.5. XPS C 1s spectra of d) N-GC-0.1, e) N-GC-0.2, and f) N-GC-0.5. g) XPS survey scan, h) real permittivity, and i) imaginary permittivity of N-GC-0.1, N-GC-0.2, and N-GC-0.5.

confirmed by XRD patterns. As shown in Figure 4a, two distinct diffraction peaks are corresponded to (002) and (001) planes of graphene. As can be seen from the FTIR spectra in Figure 4b, the C–N/C=N stretching vibration absorption appearing between 1000 and 2000  $\text{cm}^{-1}$  reveals the possible introduction of nitrogen into the carbon matrix. Elemental mapping of C (Figure 3k) and N (Figure 3l) of the selected image (Figure 3j) from N-GC-0.5 demonstrates the homogeneous distribution of nitrogen over carbon substrate. The approximately identical  $I_G/I_D$  values near 1.08 (Figure 4c) demonstrate that all the N-GC samples have nearly the same graphitization degree. Furthermore, the exhibited partial graphitization feature is in consistence with the exhibited short-range order character in the high resolution transmission electron microscopy (HRTEM)

images in Figure 3c,f. More detailed information about the nitrogen doping was studied by XPS measurements. N-species would be in situ generated during the pyrolyzing of N-containing precursors. Although oxygen functional groups may be removed during the heat treatment process, oxygen-related N-species including oxidized N are reserved.<sup>[17]</sup> As shown in the XPS N 1s spectra in Figure 4d–f, quaternary N, pyridine N, pyrrolic N, and oxidized N can all be detected. In addition, although the relative content of quaternary N dominates in all N-species, its dominance decreases as the content of N-containing precursor increases. This phenomenon can be explained as follows: the formation energy of quaternary N (0.32 eV) is the lowest among all the N-species due to its longer C–N bond length (1.39 Å) than those of pyridine N (1.33 Å) and pyrrolic N

(1.372 Å). When the feeding amount of N-containing precursor is relatively low, quaternary N is preferred. With the increase of N-containing precursor, other N-species will have more opportunity to be formed.<sup>[24,25]</sup> The total nitrogen concentration was detected by an XPS survey scan (Figure 4g), which shows the increased nitrogen doping content from N-GC-0.1 (4.50 at%) to N-GC-0.2 (5.08 at%) and N-GC-0.5 (8.39 at%). All these results indicate the successful doping of nitrogen into carbon matrix, as well as the increased nitrogen doping content from N-GC-0.1 to N-GC-0.2 and N-GC-0.5. Interestingly, the electromagnetic parameters of N-GC samples exhibit the same trend, as shown in Figure 4h,i. Based on these findings, it can be inferred that the conduction loss is dominant in determining the permittivity behaviors of materials with high conductivity (e.g., graphene, carbon nanotubes (CNTs), and Ni foam), but not the material with low conductivity like graphene oxide (GO).

As is widely known, most of the nitrogen doping can affect the electronic states of materials. Pyridinic N and pyrrolic N can contribute electron lone pairs into the carbon conjugated system. The induced electron donor effects can result in more dielectric polarizations. Quaternary N atoms will take positions inside aromatic rings with  $sp^2$  hybridization, thus enhancing the electrical conductivity of graphitized carbon.<sup>[17]</sup> Here, a  $7 \times 7 \times 1$  graphene supercell with 98 C atoms was chosen as the theoretical model to understand the influence of nitrogen doping on the electronic properties of graphitized carbon. Nitrogen doping was realized by substituting C with N atoms (quaternary N; Figure S12, Supporting Information). As shown in Figure S13 (Supporting Information), the DOSs of the nitrogen-doped graphene sheets at the Fermi level gradually increase with the increased concentration of doping nitrogen, indicating the effective modulation of nitrogen doping on the electronic structures of graphitized carbon. Electrochemical impedance spectroscopy (EIS) was first employed to investigate the electron transport characteristics of the N-GC samples. As reflected in the main panel and the inset in Figure 5a, with the concentration of doping nitrogen increases, the semicircles at high frequency decrease and the straight line slope at low frequency rises, which indicates that the conductivity is in an order of N-GC-0.1 < N-GC-0.2 < N-GC-0.5. Given that it is difficult to operate and evaluate the practical polarization process in alternating electromagnetic field at GHz, we still could not present experimental evidence to illustrate the detailed dielectric polarization process. Here, the chemical environments around C

after nitrogen doping were detected by near edge X-ray absorption fine structure (NEXAFS) experiments.<sup>[26]</sup> Near-edge X-ray absorption occurs when the core electron is excited to an unoccupied state, i.e.,  $1s \rightarrow \pi^*$  and  $1s \rightarrow \sigma^*$  transitions.<sup>[27]</sup> The spectra are characterized by four main features: the edge (atomic contribution at about 284.6 eV), a structure characterized by two peaks at 286.1 and 288.6 eV, a shoulder at about 292.4 eV, and a large magnetic spin (MS) resonance centered at about 307 eV, which are labeled as A, B, C, and D in all spectra, respectively. In general, A and C peaks are assigned to the transition from C 1s core to C–C  $\pi^*$  and  $\sigma^*$  states, respectively. The B peak is assigned to free-electron-like interlayer states in graphite or carbon nanotubes.<sup>[28]</sup> As can be seen from the NEXAFS spectra in Figure 5b, the presence of a pronounced B peak indicates structural changes with the increased  $sp^3$ -like structure, while the decreased intensity of A peaks demonstrates a weakening of the C–C  $\pi^*$  network. The changes of microscopic chemical environments/electrical states indicate the influence of nitrogen doping on the dielectric polarization process in graphitized carbon.<sup>[29]</sup>

The electrical conductivity order of N-GC-0.1 < N-GC-0.2 < N-GC-0.5 has been confirmed based on the experimental results. Interestingly, the complex permittivity values of N-GC samples also increase from N-GC-0.1 to N-GC-0.2 and N-GC-0.5. Although the detailed variation of polarization cannot be experimentally provided, some conclusions with regard to the relationship between GaP and permittivity behaviors in GC can be obtained as follows:

- i) Nitrogen doping has a positive relationship with electrical conductivity in GC.
- ii) Conduction loss is dominant in determining the dielectric behaviors of GC.

Microwave absorption properties were calculated using the measured electromagnetic parameters based on the transmission line theory<sup>[30]</sup>

$$RL = 20 \log \left| \frac{Z_{in} - Z_0}{Z_{in} + Z_0} \right| \quad (1)$$

$$Z_{in} = Z_0 \sqrt{\frac{\mu_r}{\epsilon_r}} \tanh \left( j \frac{2\pi f d}{c} \sqrt{\mu_r \epsilon_r} \right) \quad (2)$$

where  $Z_{in}$  is the input characteristic impedance,  $Z_0$  is the impedance of free space,  $d$  is the absorber thickness,  $\epsilon_r$  and  $\mu_r$  are complex permittivity and permeability,  $d$  signifies the absorber thickness, and  $c$  is the velocity of light. As can be seen from the frequency-dependent reflection loss of  $SnO_2$  and D- $SnO_2$  in Figure 6a, stannic oxide exhibits poor electromagnetic absorption performance, which originates from the inherently weak loss capacity of semiconductors. The reflection loss values of N-GC were also plotted in Figure 6b. The nitrogen-doped graphitized carbon materials show better microwave absorption performances compared to stannic oxide, their RL value gradually rises from N-GC-0.1 to N-GC-0.2 and N-GC-0.5. Cole–Cole semicircles were plotted to explore the dielectric polarization process.<sup>[31,32]</sup> As can be seen from Figures S14a–c and S15a–c (Supporting Information), D- $SnO_2$ -0.1 possesses more semicircles than  $SnO_2$  and D- $SnO_2$ -0.3, which indicates the more dielectric polarization processes in D- $SnO_2$ -0.1. The results

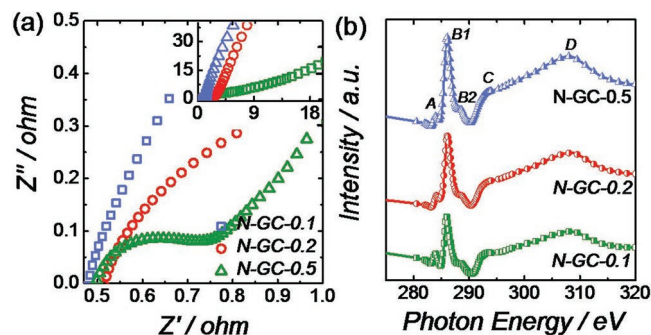


**Figure 5.** a) The close view of Nyquist plots of N-GC-0.1, N-GC-0.2, and N-GC-0.5. The inset shows the integrated Nyquist plots. b) NEXAFS C-edge spectra of N-GC-0.1, N-GC-0.2, and N-GC-0.5.

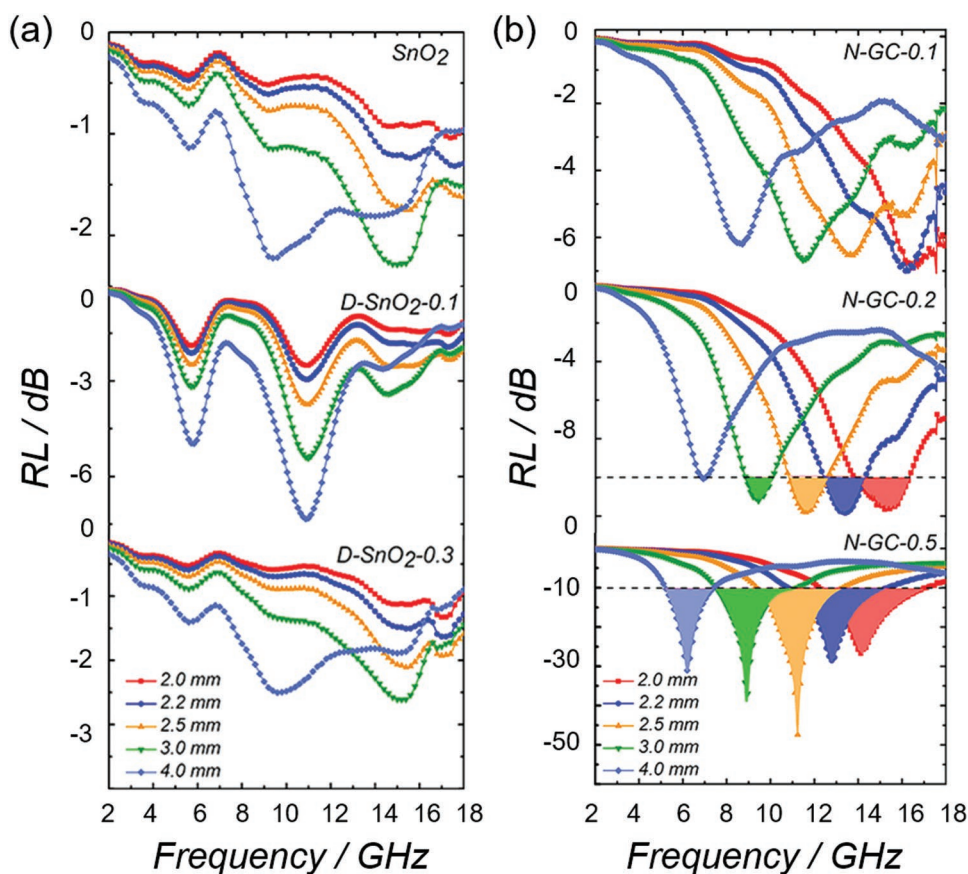


**Figure 6.** a) RL values of SnO<sub>2</sub>, D-SnO<sub>2</sub>-0.1, and D-SnO<sub>2</sub>-0.3. b) RL values of N-GC-0.1, N-GC-0.2, and N-GC-0.5.

are in accordance with the dielectric parameters and microwave absorption performances. The Cole–Cole curves of N-GC samples were also plotted in Figures S14d–f and S15d–f (Supporting Information). More semicircles in N-GC-0.2 are derived from its dielectric polarization processes, which illustrates why the real permittivity of N-GC-0.2 is higher than that of N-GC-0.5 at high frequency. However, the graphitized carbon is a conduction loss–dominated absorber, the microwave absorption performance of N-GC-0.2 is worse than that of N-GC-0.5 due to its weaker conduction loss capability. Moreover, the attenuation constant  $\alpha$  was also calculated using the measured electromagnetic parameters based on the following equation<sup>[33]</sup>

$$\alpha = \frac{\sqrt{2}\pi f}{c} \times \sqrt{(\mu''\epsilon'' - \mu'\epsilon') + \sqrt{(\mu''\epsilon'' - \mu'\epsilon')^2 + (\mu'\epsilon'' + \mu''\epsilon')^2}} \quad (3)$$

It can be found from Figure S16 (Supporting Information), the  $\alpha$  values decrease in the order of D-SnO<sub>2</sub>-0.1 > D-SnO<sub>2</sub>-0.3 > SnO<sub>2</sub>, and N-GC-0.5 > N-GC-0.2 > N-GC-0.1, respectively, which indicates the dominant role of dielectric polarization in Sc and the leading role of conduction loss in GC.

### 3. Conclusion

In summary, we have reported the introducing point defect strategy to understand the underlying relationships between

polarization/conduction loss and permittivity behaviors, where polarizability and conductivity are tunable by artificially changing the content of oxygen deficiency or heteroatom. On the basis of theoretical simulations and experimental results, we draw the following conclusions: first, dielectric polarization plays a dominant role in determining the permittivity behaviors in semiconductors due to the limited conductive capability of semiconductor materials. Second, conduction loss leads in determining the permittivity behaviors in graphitized carbon. Based on the proposed principle, we can design high-performance composite absorbers through following steps: first, improve the dielectric loss of a semiconductor to its maximum value by the proposed defect strategy; second, regulate the permittivity values of the conductor to 10–15 by the proposed defect strategy. Finally, the composite absorber with the high RL value and wide bandwidth can be achieved by moderate impedance matching, high dielectric loss capability and multiple frequency response.

### 4. Experimental Section

**Preparation of D-Sc:** The metal oxides used in this work were purchased from Nanjing Chemical Reagent Co. Typically, the aluminothermic reduction treatment was conducted in an electric tube furnace equipped with quartz tube reactors. As purchased, TiO<sub>2</sub>, SnO<sub>2</sub>, WO<sub>3</sub>, ZnO, and Fe<sub>2</sub>O<sub>3</sub> (10 mmol), and metal Al (50 nm, 0.1 g) were each ground for 30 min to obtain a uniform mixture. The mixture was then

transferred to the tube furnace with flowing Ar<sub>2</sub> (purity 99.999%), while the heating rate was controlled at 5 °C min<sup>-1</sup> and heating temperature was kept at 500 °C min<sup>-1</sup> for 3 h. In order to exclude the influence of Al nanoparticles, the as-prepared sample was washed with dilute HCl for 24 h. The used semiconductors in this work were called Sc for short, the as-obtained semiconductors treated with aluminothermic reduction were denoted as D-Sc (semiconductor with oxygen vacancies), D-Sc-0.1: aluminothermic reduction with 0.1 g Al; D-Sc-0.3: aluminothermic reduction with 0.3 g Al.

**Preparation of N-GC:** About 10 g of urea was transferred to a porcelain crucible with a lid and heated in a muffle furnace at 550 °C with a heating rate of 5 °C min<sup>-1</sup> for 4 h. After cooling to room temperature, g-C<sub>3</sub>N<sub>4</sub> was obtained. A given quantity of the as-prepared g-C<sub>3</sub>N<sub>4</sub> was dispersed in 40 mL of aqueous glucose solution (0.3 M) under sonication for 4 h. The obtained suspension was heated in Teflon autoclave at 180 °C for 10 h. The product (g-C<sub>3</sub>N<sub>4</sub>@Glucose) was collected by centrifugation, washed with deionized water and ethanol, and then dried in an oven at 60 °C for 24 h. Finally, the obtained g-C<sub>3</sub>N<sub>4</sub>@Glucose was calcined at 900 °C (5 °C min<sup>-1</sup>) for 1 h in nitrogen atmosphere. The resulting nitrogen-doped carbon was denoted as N-GC-m based on different g-C<sub>3</sub>N<sub>4</sub> addition (*m* = 0.1 g, 0.2 g, 0.5 g, respectively).

**Characterizations:** Structural characterization was carried out using XRD with a Bruker D8 Advanced X-ray diffractometer equipped with Cu K $\alpha$  ( $\lambda$  = 1.5405 Å) radiation. FTIR spectra were obtained with a Thermofisher Nicolet 6700 Fourier transformation infrared spectrometer. Raman spectra were recorded on a Raman spectrometer (Renishaw InVia). XPS information was collected by a PHI 5000 VersaProbe system with an Al K $\alpha$  X-ray source at 150 W. A UV-vis diffuse-reflectance spectrum was obtained using a UV-vis spectrometer (Shimadzu UV-3600). EPR spectra were detected at 110 K on a Bruker EMX-10/12 EPR spectrometer. EIS was conducted on a CHI 660D electrochemical workstation with a frequency range from 100 kHz to 10 MHz and an amplitude of 5 mV. The morphology of the materials was determined by a field-emission scanning electron microscope (FESEM; JEOL, JSM-6700F) and TEM (JEOL JSM-2010) equipped with energy-dispersive X-ray spectrometer (EDS). Electromagnetic parameters were tested by an Agilent PNA5244A vector network analyzer. Mass ratio between Sc/D-Sc and paraffin was 6:4 and that between N-GC and paraffin was 1:9. All samples were compacted into the same annulus ( $\Phi_{in}$ : 3.04 mm,  $\Phi_{out}$ : 7.00 mm) by the same abrasive tool to minimize the geometrical uncertainty caused error. In addition, the thickness of all the annulus was kept consistent (2.5 mm). Before the measurement, repeating calibrations were conducted until the measured electromagnetic parameters of air were within the accepted error range. Each sample was tested for several times to ensure the accuracy of *S* parameters (*S*<sub>11</sub>, *S*<sub>21</sub>). The software installed in Agilent PNA finally calculated the electromagnetic parameters automatically based on the Nicolson and Ross and Weir algorithm.

**X-Ray Absorption Fine Structure (XAFS) Measurement and Analysis:** The C K-edge X-ray absorption near edge structure (XANES) experiments were carried out at the Photoelectron Spectroscopy station of the Beijing Synchrotron Radiation Facility of the Institute of High Energy Physics, Chinese Academy of Sciences. Samples were loaded in a UHV and maintained in a background pressure of  $\approx 8 \times 10^{-10}$  Torr, reaching a pressure up to  $\approx 1 \times 10^{-9}$  Torr during data acquisition. All spectra were recorded in the energy range from 275 to 318 eV and with an experimental resolution of 0.2 eV at room temperature, using the total electron yield (TEY) mode, a surface-sensitive detection method with a typical probing depth of a few nanometers. The incident beam was set at an angle of about 45° relative to the sample surface. The annealing treatments were performed under ultra high vacuum (UHV) at about 700 K for 1 h. Photoelectron spectra were recorded with an angle-integrated hemi-spherical analyzer at an incident photon energy of 250 eV with an experimental resolution of 0.6 eV. An Ar<sup>+</sup> ion bombardment was carried out at 150 V and 20 mA beam current for 5 min.

**Computational Method:** In these theoretical calculations, the SnO<sub>2</sub> lattice was modeled using a 2 × 2 × 2 supercell with a molecular formula

of Sn<sub>16</sub>O<sub>32</sub>, and the graphene lattice was modeled using a 7 × 7 × 1 supercell with a molecular formula of C<sub>98</sub>. Here all DFT computations were implemented in the VASP code using the projector augmented wave method with the Perdew–Burke–Ernzerhof (PBE) exchange–correlation functional.<sup>[34,35]</sup> A cutoff energy of 500 eV was used for the plane-wave expansions. For structural relaxation, the Monkhorst–Pack *k*-point meshes of 4 × 4 × 6 and 3 × 3 × 1 were adopted for the unit cells of Sn<sub>16</sub>O<sub>32</sub> and graphene, respectively.<sup>[36]</sup> A 15 Å thick vacuum space was used to prevent any interactions between the adjacent periodic images of the 2D graphene. The influence of van der Waals (vdW) interactions was considered using a modified version of vdW-DF, referred to as “optB86b-vdW,” in which the PBE exchange functional of the original vdW-DF of Dion et al.,<sup>[37]</sup> was replaced with the optB86b exchange functional to yield more accurate equilibrium interatomic distances and energies for a wide range of systems. All the atoms in the unit cells are relaxed using a conjugate-gradient algorithm until the force on each atom is less than 0.01 eV Å<sup>-1</sup>. The charge polarizations were calculated using the Berry phase method as implemented in VASP.<sup>[38]</sup>

## Supporting Information

Supporting Information is available from the Wiley Online Library or from the author.

## Acknowledgements

Financial supports from the NSFC (Grant Nos. 11575085, 51602154, 11472131, and 11622218), the Aeronautics Science Foundation of China (Grant No. 2017ZF52066), the Qing Lan Project, Six talent peaks project in Jiangsu Province (Project No. XCL-035), the Jiangsu NSF (BK20160037), the program of China Scholarships Council (Grant No. 201806830013), Funding for Outstanding Doctoral Dissertation in NUAA (BCXJ 18-07), the Open Research Fund of Jiangsu Provincial Key Laboratory for Nanotechnology of Nanjing University, and the Priority Academic Program Development of Jiangsu Higher Education Institutions (PAPD) are gratefully acknowledged.

## Conflict of Interest

The authors declare no conflict of interest.

## Keywords

complex permittivity, conduction loss, dielectric materials, point defect, polarization

Received: February 10, 2019

Revised: April 8, 2019

Published online: May 8, 2019

- [1] Y. Zhang, Y. Huang, T. F. Zhang, H. C. Chang, P. S. Xiao, H. H. Chen, Z. Y. Huang, Y. S. Chen, *Adv. Mater.* **2015**, *27*, 2049.
- [2] X. F. Liu, X. Y. Nie, R. H. Yu, H. B. Feng, *Chem. Eng. J.* **2018**, *334*, 153.
- [3] H. L. Lv, Z. H. Yang, P. L. Y. Wang, G. B. Ji, J. Z. Song, L. R. Zheng, H. B. Zeng, Z. C. J. Xu, *Adv. Mater.* **2018**, *30*, 1706343.
- [4] M. Zhang, J. Zhao, Z. J. Li, S. Q. Ding, Y. Q. Wang, G. H. Qiu, A. L. Meng, Q. D. Li, *ACS Sustainable Chem. Eng.* **2018**, *6*, 3596.

- [5] D. Moitra, S. Dhole, B. K. Ghosh, M. Chandel, R. K. Jani, M. K. Patra, S. R. Vadera, N. N. Ghosh, *J. Phys. Chem. C* **2017**, *121*, 21290.
- [6] F. Ye, Q. Song, Z. C. Zhang, W. Li, S. Y. Zhang, X. W. Yin, Y. Z. Zhou, H. W. Tao, Y. S. Liu, L. F. Cheng, L. T. Zhang, H. J. Li, *Adv. Funct. Mater.* **2018**, *28*, 1707205.
- [7] X. C. Lu, W. J. Bian, Y. Y. Li, H. K. Zhu, Z. X. Fu, Q. T. Zhang, *J. Am. Ceram. Soc.* **2018**, *101*, 1646.
- [8] X. C. Lu, W. J. Bian, C. F. Min, Z. X. Fu, Q. T. Zhang, H. K. Zhu, *Ceram. Int.* **2018**, *44*, 10028.
- [9] H. L. Xu, X. W. Yin, M. H. Li, F. Ye, M. K. Han, Z. X. Hou, X. L. Li, L. T. Zhang, L. F. Cheng, *Carbon* **2018**, *132*, 343.
- [10] T. Wu, Y. T. Zhao, Y. N. Li, W. H. Wu, G. X. Tong, *ChemCatChem* **2017**, *9*, 3486.
- [11] B. Quan, X. H. Liang, G. B. Ji, Y. Cheng, W. Liu, J. N. Ma, Y. N. Zhang, D. R. Li, G. Y. Xu, *J. Alloys Compd.* **2017**, *728*, 1065.
- [12] H. J. Yang, W. Q. Cao, D. Q. Zhang, T. J. Su, H. L. Shi, W. Z. Wang, J. Yuan, M. S. Cao, *ACS Appl. Mater. Interfaces* **2015**, *7*, 7073.
- [13] X. J. Zhao, W. P. Liu, X. B. Jiang, K. Liu, G. R. Peng, Z. J. Zhan, *Mater. Res. Express* **2016**, *3*, 075304.
- [14] Z. G. Geng, X. D. Kong, W. W. Chen, H. Y. Su, Y. Liu, F. Cai, G. X. Wang, J. Zeng, *Angew. Chem., Int. Ed.* **2018**, *57*, 1.
- [15] P. Ge, C. Y. Zhang, H. S. Hou, B. K. Wu, L. Zhou, S. J. Li, T. J. Wu, J. G. Hu, L. Q. Mai, X. B. Ji, *Nano Energy* **2018**, *48*, 617.
- [16] T. Zhang, M. Y. Wu, D. Y. Yan, J. Mao, H. Liu, W. B. Hu, X. W. Du, T. Ling, S. Z. Qiao, *Nano Energy* **2018**, *43*, 103.
- [17] M. Yang, Z. Zhou, *Adv. Sci.* **2017**, *4*, 1600408.
- [18] S. Deepa, K. P. Kumari, B. Thomas, *Ceram. Int.* **2017**, *43*, 17128.
- [19] G. Ou, Y. S. Xu, B. Wen, R. Lin, B. H. Ge, Y. Tang, Y. W. Liang, C. Yang, K. Huang, D. Zu, R. Yu, W. X. Chen, J. Li, H. Wu, L. M. Liu, Y. D. Li, *Nat. Commun.* **2018**, *9*, 1302.
- [20] H. P. Dang, Q. H. Luc, V. H. Le, T. Le, *J. Alloys Compd.* **2016**, *687*, 1012.
- [21] L. W. Zhang, H. H. Mohamed, R. Dillert, D. Bahnemann, *J. Photochem. Photobiol., C* **2012**, *13*, 263.
- [22] J. Zheng, G. B. Ji, P. Zhang, X. Z. Cao, B. Y. Wang, L. H. Yu, Z. C. Xu, *Chem. - Eur. J.* **2015**, *21*, 18309.
- [23] G. Kresse, J. Furthmüller, *Phys. Rev. B* **1996**, *54*, 11169.
- [24] W. J. Lee, J. Lim, S. O. Kim, *Small Methods* **2017**, *1*, 1600014.
- [25] T. Sharifi, G. Z. Hu, X. E. Jia, T. Wågberg, *ACS Nano* **2012**, *6*, 8904.
- [26] W. G. Liu, L. L. Zhang, W. S. Yan, X. Y. Liu, X. F. Yang, S. Miao, W. T. Wang, A. Q. Qang, T. Zhang, *Chem. Sci.* **2016**, *7*, 5758.
- [27] P. Y. Zhu, J. X. Song, D. P. Lv, D. H. Wang, C. Jaye, D. A. Fischer, T. P. Wu, Y. S. Chen, *J. Phys. Chem. C* **2014**, *118*, 7765.
- [28] J. Zhong, L. Song, Z. Y. Wu, S. S. Xie, M. Abbas, K. Ibrahim, H. J. Qian, *Carbon* **2006**, *44*, 866.
- [29] S. K. Nayak, C. J. Hung, V. Sharma, S. P. Alpay, A. M. Dongare, W. J. Brindley, R. J. Hebert, *npj Comput. Mater.* **2018**, *4*, 11.
- [30] B. Quan, X. H. Liang, G. B. Ji, J. N. Ma, P. Y. Ouyang, H. Gong, G. Y. Xu, Y. W. Du, *ACS Appl. Mater. Interfaces* **2017**, *9*, 9964.
- [31] T. K. Gupta, B. P. Singh, V. N. Singh, S. Teotia, A. P. Singh, I. Elizabeth, S. R. Dhakate, S. K. Dhawanc, R. B. Mathur, *J. Mater. Chem. A* **2014**, *2*, 4256.
- [32] B. Quan, X. H. Liang, G. B. Ji, Y. N. Zhang, G. Y. Xu, Y. W. Du, *ACS Appl. Mater. Interfaces* **2017**, *9*, 38814.
- [33] X. J. Zhang, J. Q. Zhu, P. G. Yin, A. P. Guo, A. P. Huang, L. Guo, G. S. Wang, *Adv. Funct. Mater.* **2018**, *28*, 1800761.
- [34] B. Hammer, L. B. Hansen, J. K. Nørsko, *Phys. Rev. B* **1999**, *59*, 7413.
- [35] P. E. Blöchl, *Phys. Rev. B* **1994**, *50*, 17953.
- [36] H. J. Monkhorst, J. D. Pack, *Phys. Rev. B* **1976**, *13*, 5188.
- [37] M. Dion, H. Rydberg, E. Schröder, D. C. Langreth, B. I. Lundqvist, *Phys. Rev. Lett.* **2004**, *92*, 246401.
- [38] R. D. King-Smith, D. Vanderbilt, *Phys. Rev. B* **1993**, *47*, 1651.